PCCP



PAPER View Article Online



Cite this: Phys. Chem. Chem. Phys., 2021. 23, 6880

Data-driven analysis of the electronic-structure factors controlling the work functions of perovskite oxides†

Yihuang Xiong, (1) * Weinan Chen, Wenbo Guo, Hua Wei and Ismaila Dabo (1) ac

Tuning the work functions of materials is of practical interest for maximizing the performance of micro-electronic and (photo)electrochemical devices, as the efficiency of these systems depends on the ability to control electronic levels at surfaces and across interfaces. Perovskites are promising compounds to achieve such control. In this work, we examine the work functions of more than 1000 perovskite oxide surfaces (ABO₃) using data-driven (machine-learning) analysis and identify the factors that determine their magnitude. While the work functions of the BO₂-terminated surfaces are sensitive to the energy of the hybridized oxygen p bands, the work functions of the AO-terminated surfaces exhibit a much less trivial dependence with respect to the filling of the d bands of the B-site atom and of its electronic affinity. This study shows the utility of interpretable data-driven models in analyzing the work functions of cubic perovskites from a limited number of electronic-structure descriptors.

Received 26th October 2020, Accepted 26th February 2021

DOI: 10.1039/d0cp05595f

rsc.li/pccp

1 Introduction

The work function measures the energy of extracting an electron from a material. Understanding trends in the work function is technologically important to thermionics, optoelectronics, electrochemistry, and photocatalysis, 2-8 - with one primary example being the possibility to optimize the activity of a surface by tuning its electronic affinity.9 Perovskites are a remarkably versatile class of materials that can be synthesized with controlled purity and relatively high yield. 10-12 Due to the interplay between their structural, chemical, and electronic characteristics, perovskites are promising candidates for achieving sensitive control of the work function. Fig. 1 compares the work functions of elemental metals¹³ with those of perovskite oxides; it is apparent that perovskites show a wide distribution of work functions, providing a rich compositional space for the design of e.g. thermionic converters (requiring low work functions)14 and photovoltaic hole collectors (requiring high work functions).

In this work, we develop a data-driven understanding of the work functions of perovskite oxides in their prototypical cubic symmetry. For comparison, Fig. 2 shows the work functions of 10 representative perovskites in the orthorhombic (Pnma) and cubic ($Pm\bar{3}m$) phases along their [001] surface facets. These results highlight a strong correlation between the work functions of these structures, indicating that the high-symmetry, cubic phase may provide a reliable basis to infer the work functions of low-symmetry, perovskite-related structures featuring octahedral rotations. Examining cubic structures is also relevant to high-entropy perovskites¹⁵ that tend to spontaneously adopt high symmetry. ^{15,16} We thus present a detailed analysis of the dependence of the work

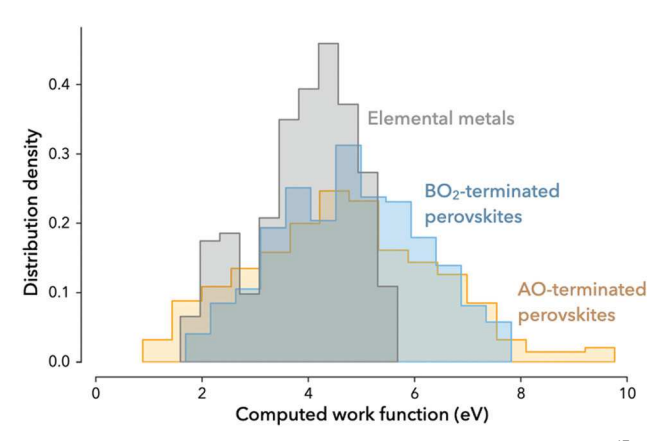


Fig. 1 Distribution of the computed work functions for elemental metals¹³ and cubic perovskites. Perovskites show a broad distribution of work functions.

^a Department of Materials Science and Engineering, and Materials Research Institute, The Pennsylvania State University, University Park, PA, USA. E-mail: yihuangxiong@psu.edu

b College of Information Sciences and Technology, The Pennsylvania State University, University Park, PA 16802, USA

^c Institutes of Energy and Environment, The Pennsylvania State University, University Park, PA 16802, USA

 $[\]dagger$ Electronic supplementary information (ESI) available: A schematic of a regression tree in the random forests, feature selections based on the correlation matrix and importance ranking, and the projected density of states of the selected perovskites. See DOI: 10.1039/d0cp05595f

Paper

Pnma BO₂ termination Work function of Pnma perovskites (eV) $R^2 = 0.929$ RMSE = 0.327Pm3m AO termination 2

Fig. 2 Comparison of the computed work functions along the [001] direction for a representative set of 10 perovskite oxides with space groups $Pm\bar{3}m$ and Pnma. The selected compositions are ABO₃ where A = Ca or Sr and B = Ti, V, Cr, Mn or Fe. The overall coefficient of determination (R^2) and root mean squared error are of 0.929 and 0.237 eV, respectively.

Work function of Pm3m perovskites (eV)

functions of cubic perovskites as a function of composition and termination using extensive computational data.

2 Computational method

2.1 Crystal structures and first-principles calculations

A perovskite crystal structure with formula ABO₃ is shown in Fig. 3. The B-site cation is octahedrally coordinated to oxygen, and, typically, a larger A-site cation adopts a twelve-fold coordination with the surrounding oxygen atoms. The cubic perovskite phase exists in nature (e.g. SrTiO₃ and SrVO₃), while many other lower-

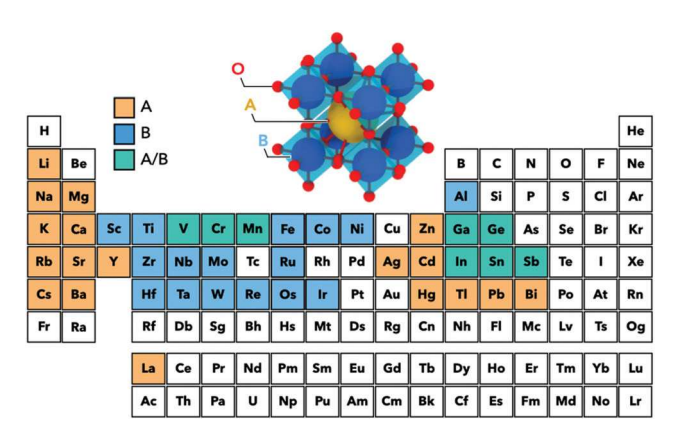


Fig. 3 A perovskite unit cell is composed of the A cation at the center of the unit cell, and the B cation octahedrally coordinated with the oxygen (top). The elemental compositions that are used to construct the perovskites are highlighted in the periodic table (bottom).

symmetry stable structures are also found. Compared to the ideal cubic structure, distortions such as octahedral rotations and cations displacements may occur, and some of them are responsible for functional properties such as ferroelectricity. 17 Nevertheless, we adopt the cubic phase as a simple template for statistical analysis, as discussed above and justified in Fig. 2.

Following ref. 18 and 19, we select the constituent metal cations based on their propensity to form a stable cubic phase. The elements that are considered in this work are highlighted in Fig. 3. The A-site elements include the main-group metals, while the majority of the B-site elements belong to the transition metal series. Considering the alternating AO and BO2 layers, we construct two types of interfaces along the [001] direction, as shown in Fig. 4. Using the optimized bulk structures, each slab geometry is built symmetrically with 9 ionic layers. The periodic slabs are separated by 14 Å of vacuum. Only the two outermost layers are allowed to move during geometry optimization.

All first-principles calculations are managed using the AiiDA high-throughput calculation infrastructure.²⁰ The self-consistentfield calculations are performed at the semilocal Perdew-Burke-Ernzerhorf (PBE) level²¹ using the pw code of the Quantum ESPRESSO distribution.²² Ionic cores are represented by normconserving pseudopotentials with a kinetic-energy cutoff of 100 Ry for the reciprocal-space expansion of the wave functions.²³ Bulk structures are fully optimized through variable-cell calculation, while sampling the Brillouin zone with a Γ-centered Monkhorstpack grid of $12 \times 12 \times 12.^{24}$ For slab calculations, a Marzari-Vanderbilt cold smearing of 0.01 Ry²⁵ is employed to discretize the Brillouin zone with a reduced k-point mesh of $6 \times 6 \times 1$. In addition, the Environ module is applied to automatically align the Fermi level with respect to vacuum. 26-28 The atomic positions are then fully optimized until the interatomic forces became smaller than 0.02 eV Å^{-1} .

Based on the optimized perovskite surface, we can calculate the work functions as

$$\Phi = \Phi^{\circ} - E_{\rm F},\tag{1}$$

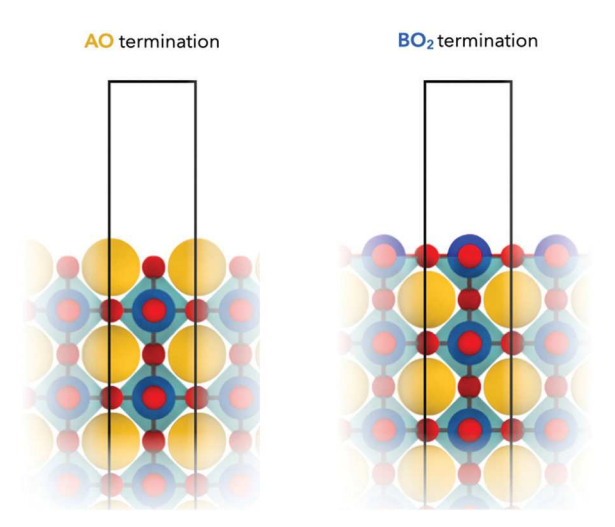


Fig. 4 Surface structures considered in this work: the AO and BO₂ terminations.

where Φ° is the potential in a vacuum and E_{F} is the Fermi energy.

Due to the semilocal PBE approximation, the calculated band gap and work function are expected to be underestimated. 13,29 Even though previous work suggests that the work functions of metals calculated from PBE are consistent with experimental measurements, 13,30 there is still a debate about the accuracy of PBE work functions for perovskite oxides. More generally, the work functions of metal oxides can be strongly influenced by surface orientations, terminations, and defects. Studies of Ma et al. and Guo et al. showed that an accurate description of band gaps could lead to improved predictions of the work functions and band edges of semiconductors. 31,32 Although predicting absolute work functions using the PBE functional may not be accurate, Ma et al. and Chambers and Sushko showed that the PBE approximation is reliable to estimate differences in the work functions of AO and BO₂-terminated surfaces. 32,33 While beyond the scope of this work, it is expected that hybrid functionals such as Heyd-Scuseria-Ernzerhof (HSE)34 could be more accurate for evaluating the work functions of perovskite metal oxides. Since the goal of this study is to understand trends between work functions and electronic descriptors, we argue that it is suitable to use the PBE functional.

2.2 Machine-learning method and descriptor selection

On the basis of our computed datasets, we aim to identify the features that best describe the work functions of the perovskites. To achieve this, we employ a statistical learning method. We chose our model based on interpretability and performance. Here, we use random forest regression,35 which is an ensemble statistical learning method that integrates a number of decision trees and that returns the average prediction of these trees.³⁶ In specific terms, given a training set (X, y) where X is the features and y are the corresponding responses, the random forest model is trained by repeatedly sampling a subset x of the training set to form the trees. The quality of the branch split is measured using the mean squared error (MSE) of the

regression: MSE =
$$\frac{1}{N} \sum_{n=1}^{N} (y_n - \hat{y}_n)^2$$
.

For each testing sample x, the prediction is obtained from the averaged prediction of the individual trees: $f(\mathbf{x}) = \frac{1}{M} \sum_{m=1}^{M} f_m(\mathbf{x})$,

where M is the total number of trees and f_m stands for the prediction of each tree model using data x. Random forests are known to be robust against overfitting, and have been widely applied for both regression and classification tasks.³⁷ In addition, random forests offer a means of interpreting the model using importance ranking and partial dependence analysis. 38,39 To train the model for predicting the work function, we 'fingerprint' the interface structures in our database with a number of features that are physically meaningful and are expected to be correlated with the work functions. Some of the selected features have been shown previously to be critical to describe phase stability, 40 thermal conductivity,⁴¹ optical absorption,^{42,43} superconductivity,⁴⁴ catalytic activity, 45 and fuel-cell performance. 46 In total, 38 features are selected and summarized in Table 1.

All features, except \bar{E}_{2p}^{O} and $\chi_{\rm ABO_3}^{ABO_3}$, are selected for both A and B elements. We computed the ionization potential IPcalc and the electron affinity EA_{calc} of the atoms using the energy of the half occupied Kohn-Sham orbital.49 Furthermore, the band center of orbital φ is the energy difference between the weighted center of the φ -projected band and the Fermi level in a crystal:

$$\bar{E}_{\varphi} = \frac{\int_{-\infty}^{\infty} E \rho_{\varphi}(E) dE}{\int_{-\infty}^{\infty} \rho_{\varphi}(E) dE} - E_{F}, \tag{2}$$

and the filling factor of the φ band (similarly for e_g and t_{2g} bands) is calculated from

$$\theta_{\varphi} = \frac{\int_{-\infty}^{E_{F}} \rho_{\varphi}(E) dE}{\int_{-\infty}^{\infty} \rho_{\varphi}(E) dE},$$
(3)

where ρ_{φ} stands for the projected density of states of the φ orbital. This projection is expressed as

$$\rho_{\varphi}(E) = \frac{1}{N_{\mathbf{k}}} \sum_{n\mathbf{k},\sigma} \int \left| \left\langle \psi_{n\mathbf{k}}^{\sigma} | \varphi \right\rangle \right|^{2} \delta(E - E_{n\mathbf{k}}^{\sigma}) dE, \tag{4}$$

where n, \mathbf{k} and σ denote the band index, \mathbf{k} -points and the spin states of the wave function ψ , respectively.

Table 1 Atomic descriptors that are selected in this work

Notation	Definition
IP _{expt} , EA _{expt} , IP _{calc} , EA _{calc} $ \begin{array}{l} \chi_{\rm P} \\ \delta \\ r_{\rm s}, r_{\rm p}, r_{\rm d} \\ R_{\rm atm.}, \bar{R}_{\rm ion} \\ P \\ Z \\ M \\ \bar{E}_{\rm p} \end{array} $	Experimental and calculated ionization potential and electron affinity Pauling electronegativity Bonding covalency with oxygen s, p and d valence orbital radii of the element ⁴⁷ Atomic radii and averaged ionic radii Pettifor's chemical scale ⁴⁸ Atomic number Mendeleev number p band center in the bulk perovskite Filling factor of the d band, e _g and t _{2g} in the bulk perovskite Center of the oxygen 2p band in the bulk perovskite
$egin{aligned} heta_{ m d}, \; heta_{ m eg}, \; heta_{ m t2g} \ ilde{E}_{ m 2p}^{ m O} \ ilde{\lambda}^{ m ABO}_3 \ ilde{\chi}_{ m M} \end{aligned}$	Geometric mean of the electronegativity of the perovskite constituents on a Mulliken scale

We note that the inclusion of DFT features requires some initial bulk calculations. Constructing models using only readily available features such as the elemental properties 50-52 would overcome this requirement; however, these DFT features enable us to establish closer correlation between the work functions and electronic-structure properties, as further analyzed and discussed below.

3 Results and discussion

3.1 Random forest regression

We develop the random forest models using the scikit-learn library.⁵³ The dataset contains 1248 interface work functions and is composed of an equal amount of AO and BO₂ surfaces. Two models are trained independently of the work functions of the AO and BO₂ terminations. Before training the models, we note that some of the selected features are correlated. Although such correlations would not impact the performance of the model, they could deteriorate its interpretability. This is because the correlated features carry similar information, thus the feature importance would be shared among them, causing a 'dilution' of the importance score across the feature group. Therefore, we carried out a reduction of the feature dimension using the Pearson correlation analysis, as detailed in Fig. S1 (ESI†). This process reduces the number of features from 38 to 21 by eliminating the most highly correlated ones. We start the analysis by using all the features to train the random forest regression models. For both AO and BO2 terminations, we partition the dataset into 80% and 20% for training and test sets. Using the training set, the hyperparameters that give the lowest root mean squared error (RMSE) are selected. The RMSE is evaluated with fivefold cross-validations. The obtained model performance is then validated using only the test set. Such an evaluation is repeated 40 times by shuffling the datasets to obtain an averaged total performance. By doing so, we can consistently evaluate the accuracy of the model.

We first aim to identify the features that are relevant to the work functions. This is achieved by examining their importance score. In specific terms, the importance of a feature measures how much the feature would impact the predictions. For example, we can calculate the importance of a feature by adding up the weighted variance reduction for all nodes that use this feature as the splitting feature, and then averaged over the trees in the trained forests. Based on the importance score, we perform recursive feature elimination, 43,44 and then re-train the model each time to obtain a new importance ranking. To optimize the performance of the model when each feature is removed, the hyperparameter is re-selected using the aforementioned process. The resulting model contains a compatible hyperparameter and a number of features. The averaged RMSE of the regression with respect to the number of features is shown in Fig. S2 (ESI†), along with detailed descriptions of the model constructing process. We found that the averaged RMSE values of the work function of AO and BO2 terminations are 0.468 eV and 0.531 eV, respectively. The averaged predicted

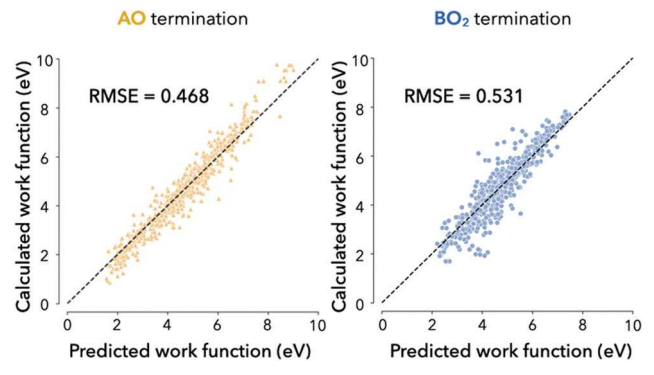


Fig. 5 Predicted versus computed work functions of AO and BO₂ terminations. The performance of the random forest regression models is evaluated by averaging the results from randomly shuffled datasets. The averaged root mean squared error for AO and BO₂ terminations are 0.468 eV and 0.531 eV, with standard deviations of 0.047 eV and 0.048 eV, respectively.

work function Φ values are plotted against the DFT values in Fig. 5(a and b). The prediction accuracy is reasonable considering that the work functions span a range of 9 eV. For the six most predominant features that are identified in the models, we summarize their normalized feature importance in Fig. 6.

Based on the importance ranking, we find that the most relevant features for both surfaces show a consistent pattern despite the different surface structures. For the BO2 terminations, the work function is strongly influenced by the bulk 2p band center of oxygen \bar{E}_{2p}^{O} , which has an importance score of 0.44. Following that, two features that are related to the terminated element, namely $r_{\rm d}^{\rm B}$ and ${\rm P}^{\rm B}$, are found to be relatively important for the work functions of BO₂ terminations. This indicates that the work function of BO2 is largely determined by its bulk properties. On the other hand, though \bar{E}_{2p}^{O} is still relevant to the AO work functions, it only ranked as the

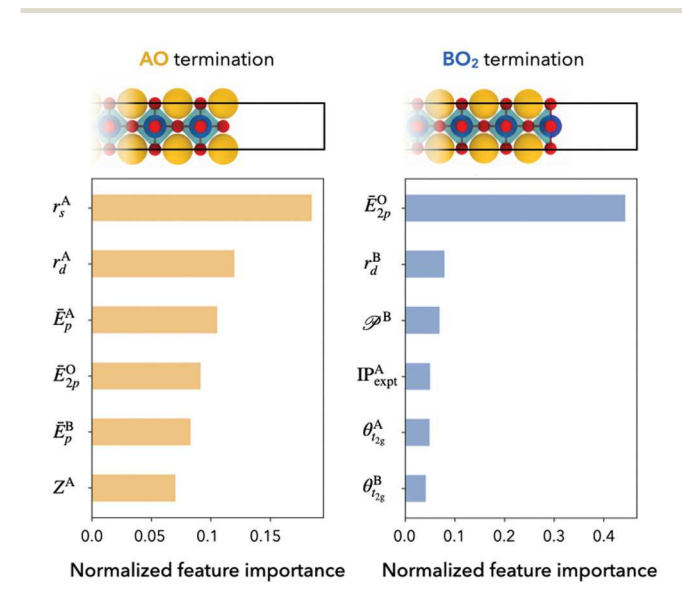


Fig. 6 Normalized feature importance of the 6 most relevant features for AO and BO₂ terminations.

fourth most important feature. The first three features are consistently correlated with the surface species of AO terminations; they are r_s^A , r_d^B , and \bar{E}_p^A . This result shows that, in contrast to BO₂ surfaces, the surface contribution to the work function is more significant than the bulk properties for the AO terminations.¹⁴ In general, the machine-learning models correctly recognize the termination effect, where the valence orbital radii for A and B elements are predicted to be among the most essential features for the AO and BO2 terminations. In addition, it is known that the work function is influenced by both bulk and surface properties. 14,54,55 The machine-learning models correctly capture this dependence.

It is interesting to note that, for both AO and BO2 terminations, the energy of the oxygen 2p orbital in the bulk phase plays a critical role. In fact, \bar{E}_{2p}^{O} is an important bulk electronic predictor that has been used to describe many electronic properties of perovskites, including vacancy formation energies,⁵⁶ oxygen reduction reactivity of oxide fuel cells⁴⁶ and oxygen evolution reactivity. 57,58 Specifically for work functions, Jacobs et al. have reported \bar{E}_{2p}^{O} as a critical descriptor by exploring 20 technologically relevant perovskite materials that are composed of Sr and La for the A atoms and 3d transition metals for the B atoms. Here, our data-driven approach corroborates that \bar{E}_{2p}^{O} remains an effective descriptor even for a wide range of metastable perovskites.

Although it helps identify the most significant features, the importance score only indicates how much the predictions are affected by the features, without explaining the specific relationship. To answer this question, we conduct a partial dependence analysis³⁹ for the two most predominant features. Partial dependence plots (PDP) illustrate the marginal effect (in the probabilistic sense) of the selected features on the predictions after integrating out the other variables. If we only focus on one specific feature x, the interactions between x and the response of the target can be estimated by marginalizing the predictions over all other features. This partial dependence function $\bar{f}_s(\mathbf{x})$ can be expressed as

$$\bar{f}_{s}(\mathbf{x}) = \frac{1}{N} \sum_{n=1}^{N} f(x_{1,n}, \dots, x_{s-1,n}, x, \dots, x_{M,n}),$$
 (5)

where $\bar{f}_s(\mathbf{x})$ is approximated by averaging the output of the trained model for all features except the selected feature $x = x_s$ in the dataset. M is the total number of features in the model, and N is the total number of samples. Similar to the previous analysis, the PDP is obtained by averaging the results using the shuffled datasets. In Fig. 7, we illustrate the PDP for both AO and BO_2 work functions with respect to \bar{E}_{2p}^O and the valence orbital radii $r_{\rm s}^{\rm A}$ and $r_{\rm d}^{\rm B}$.

Despite different surface structures, we found that the general trend of how \bar{E}_{2p}^{O} influences Φ is universal, as shown in Fig. 7(a): with a larger separation between \bar{E}_{2p}^{O} and the Fermi level (more negative band center of O 2p in the bulk), the work function shows an approximately monotonic decrease. Interestingly, such a correlation starts to break down for the perovskite interfaces with low work functions, where the work

function reaches a plateau when \bar{E}_{2p}^{O} is below -4 eV, especially for AO termination. To explain these trends, we examine the density of states, and the correlations between \bar{E}_{2p}^{O} and the work function. In general, the low work function of a perovskite originates from low filling of the d bands, as shown in Fig. 8(a). One of the representative compounds of this class is SrVO₃. ¹⁴ Thus, as we move across the 3d transition metal series, the d bands are filled up with electrons and move down to hybridize with the O 2p band. This can also be understood by analyzing electron affinities. A more electronegative B site will create a more covalent bond with oxygen, thus leading to more pronounced band hybridization. A key characteristic for such a hybridization is that, the band center of oxygen 2p is almost unchanged with respect to the vacuum level [see Fig. S5(a), ESI†]. This observation is consistent with previous literature¹⁴ and enables one to understand the linear correlation between \bar{E}_{2p}^{O} and the work functions: with increasing d filling, the d bands hybridize with the O 2p bands and reduce the energy separation between the Fermi level and the O 2p band center. Since \bar{E}_{2p}^{O} remains almost constant with respect to the vacuum level (indicating moderate charge transfer between the inner and outer layers), a decrease in the Fermi level and an increase in the work function are observed.

Yet, we observe that the previously described correlation breaks down for deep \bar{E}_{2p}^{O} levels. To understand these deviations, we examined the compounds with \bar{E}_{2p}^{O} deeper than -4 eV and found that those perovskites primarily contain 5d elements, such as Ta, W and Re. By examining their projected density of states [see Fig. S5(b), ESI†], we found that the key difference lies in the stability of the band center for O 2p. In this case, it is observed that \bar{E}_{2p}^{O} is no longer constant (indicating charge transfer between the inner and outer layers), as depicted in Fig. 8(b) by the shift of \bar{E}_{2p}^{O} towards the vacuum energy level. This trends explain the loss of correlation between the \bar{E}_{2p}^{O} level and the work function of those compounds. We further study this trend by examining the partial dependence of the work function with respect to \bar{E}_{2p}^{O} and r_{s}^{A} for the AO termination in Fig. 7(b). It is apparent that when \bar{E}_{2p}^{O} is above -4 eV, the isocontours align horizontally, which indeed confirms the strong correlation between $\bar{\it E}_{\rm 2p}^{\rm O}$ and the work functions. In contrast, the isocontours are mostly vertical when \bar{E}_{2p}^{O} is deeper than -4 eV.

Next, we turn our attention to the influence of the valence orbital radii on the work function. We first discuss the AO termination, and we highlight different groups of elements in Fig. 7(c). We found that the work function can be parsed into three regions: (1) $r_{sp}^{A} < 1.0$ Bohr, (2) 1.0 Bohr $< r_{s}^{A} < 1.3$ Bohr, and (3) $r_s^A > 1.3$ Bohr. In fact, these three regions correspond to alkali/alkaline-earth metals, transition metals, and post-transition metals and metalloids. The valence orbital radii have been shown to capture the periodic trends, 47 except for Li and Na due to their small radii. For elements belonging to the family of posttransition metals and metalloids, the work function tends to decrease with respect to the increase of the valence orbital radii. This can be explained in terms of the electronegativity: alkali/ alkaline-earth metals (larger r_s^A) show lower electronegativity

Paper

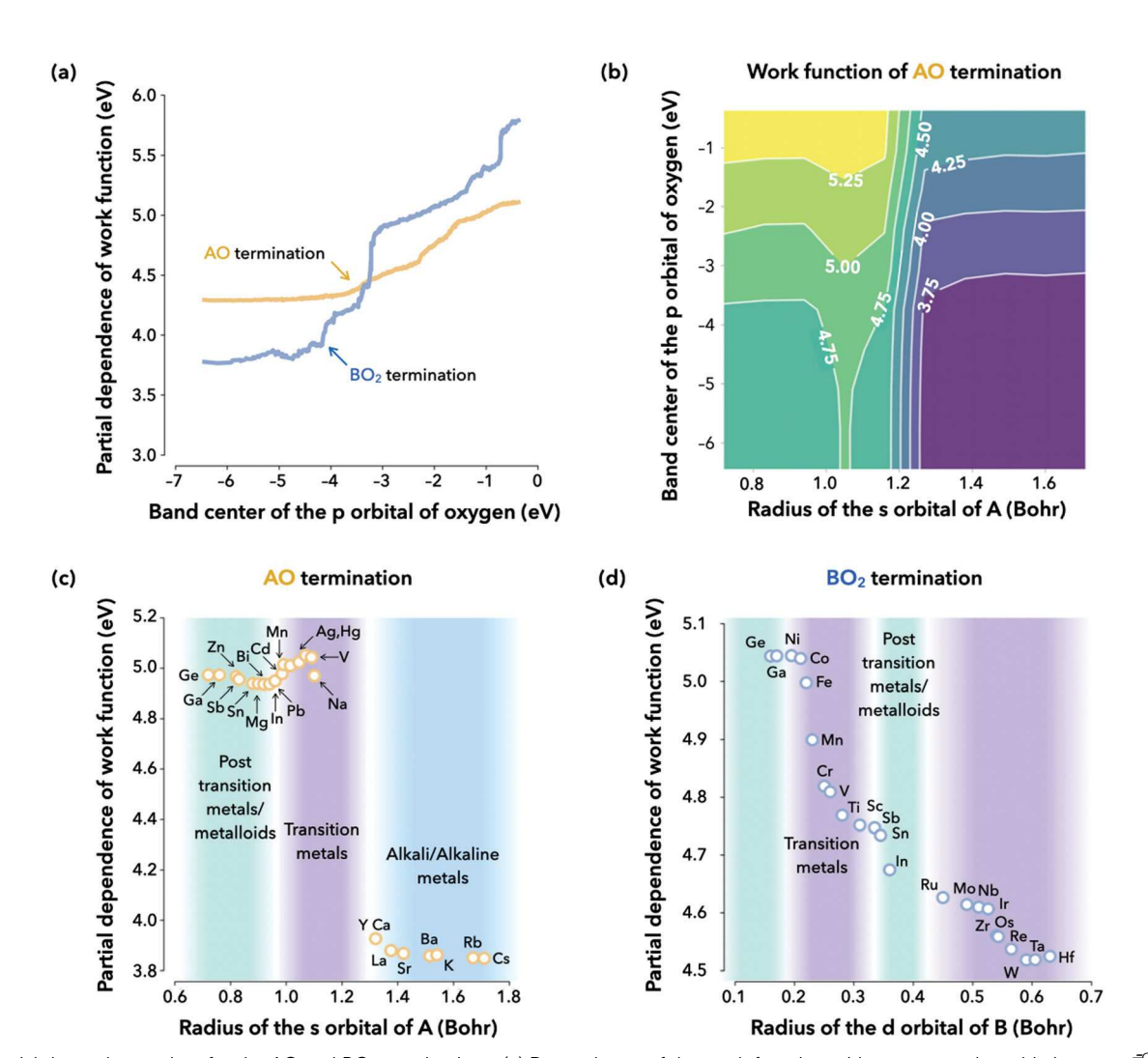


Fig. 7 Partial dependence plots for the AO and BO₂ terminations. (a) Dependence of the work function with respect to the orbital energy \vec{E}_{20}° for both interfaces. (b) Two-variable dependence plots of the work functions of both orbital energy $\bar{E}_{2p}^{\mathbb{Q}}$ and the orbital radius $r_s^{\mathbb{A}}$ for AO-terminated interfaces. (c and d) Partial dependence of the work function with respect to the radius of the p(d) orbital of the A (B) element for the AO (BO₂) termination. The colored regions represent groups of elements in the periodic table.

compared to that of post-transition metals and metalloids (smaller r_s^A), thereby yielding smaller work functions. In addition, because of our choice of A cation across the periodic table, we observe a clear separation of the work function between surfaces that are terminated with alkali/alkaline-earth metals and the posttransition metals/metalloids. The low work function of the alkali/ alkaline terminated perovskites makes them potential candidates for designing thermionic converters.

We can now discuss the trend between the size of the d orbital radii of the B atoms (r_d^B) and the work function of BO₂ surfaces with similar arguments. Fig. 7(d) shows that the work functions also decrease with $r_{\rm d}^{\rm B}$. The increasing $r_{\rm d}^{\rm B}$ radii reflect a decrease in electronegativity, thus causing a diminution in the work function. Compared to the PDP of the AO surface, we do not observe significant separation in the dependence of the work functions as a function of BO₂ surface interactions. This is likely due to the fact that the B cations are mainly transition metals and metalloids, with no alkaline/alkali metals included. These partial dependence analyses reveal that the work function is determined by both bulk electronic properties and surface electronegativity. By controlling compositions and structures, these two effects can be leveraged simultaneously to design materials with desired work functions.

In closing, we underscore the practical importance of our statistical observations. A low work function is a crucial requirement for designing electron emitters and thermionic energy converters, and we find here that perovskites with alkali or alkaline-earth metals at the A site are promising candidates for these applications, as shown in Fig. 7. We conclude that although the center of the oxygen 2p band is a sensitive descriptor of the work function for a number of perovskites, AO-terminated surfaces with shallow Fermi energy are much better described by the orbital radii of the A-site elements. This analysis demonstrates the possibility of optimizing the surface structure and chemistry to effectively reduce the work function for e.g. thermionic energy conversion.

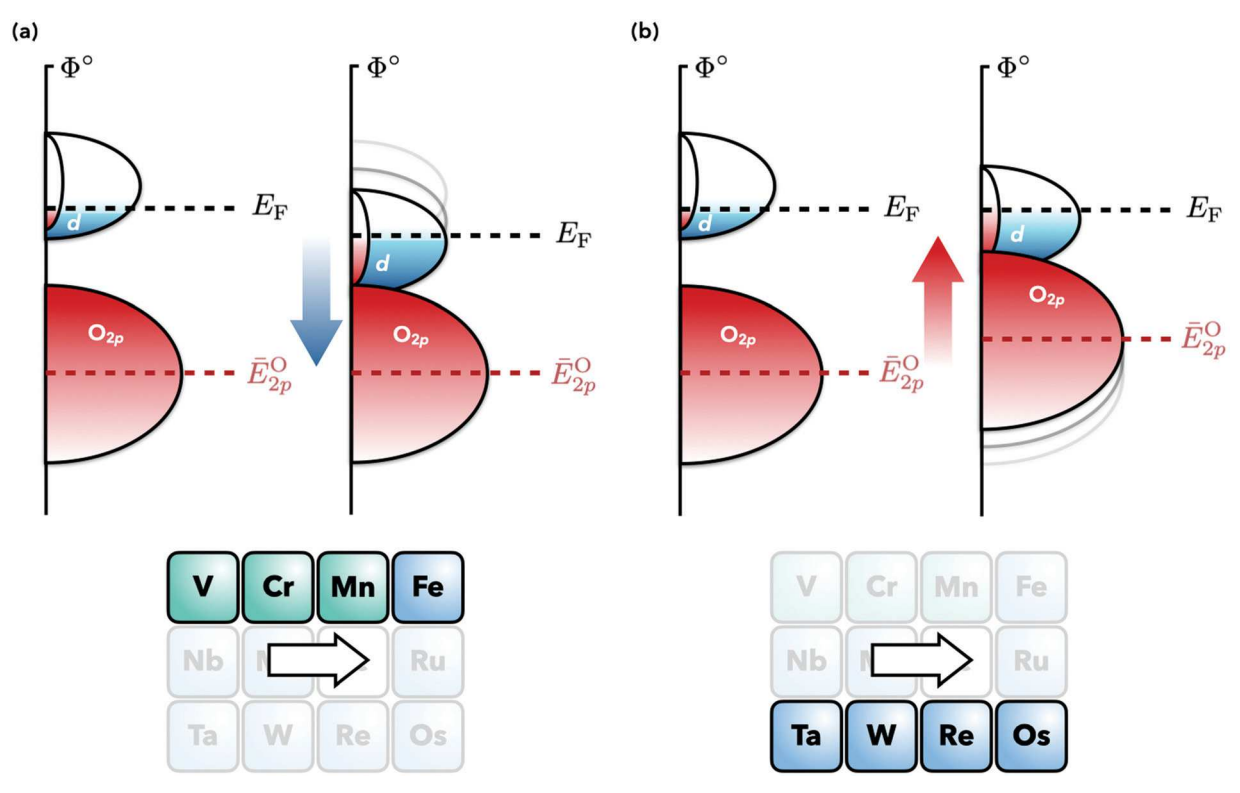


Fig. 8 Schematized densities of states for perovskites that contain (a) 3d transition metals and (b) 5d transition metals. Φ° stands for the energy level of vacuum. The red and blue regions correspond to the p and d bands of oxygen and of the B-site transition metal, respectively. The black and red dashed lines represent the Fermi level and the O 2p band center, respectively.

4 Conclusions

We have examined the work functions of cubic perovskites by statistical means. We have constructed a database of perovskites and have employed a random forest regression to predict their work functions, achieving predictive accuracy with only a few features included. Two central features that primarily control the perovskite work functions have been identified: the oxygen 2p band center and the valence orbital radii of the surface-terminating cations. The oxygen 2p band center is found to be crucial to the determination of the BO2termination work functions, while r_s^A predominantly influences the AO-termination work functions. We have explained how those electronic descriptors affect the work functions of perovskites using partial dependence analysis, and have found that the general trends are related to the stability of oxygen energy levels and atomic electronegativities. These correlations may benefit the search for metal oxides with desired surface electronic properties. For instance, optimizing the compositions of the perovskites to achieve deep oxygen 2p band centers while simultaneously terminating the interface with alkali or alkaline-earth elements may yield optimally low work functions, which are essential for thermionics. Conversely, the perovskites that have shallow oxygen 2p band centers, coupled with p-block metal or metalloid terminations, may be of interest for designing hole collectors.

Data availability

The work-function and descriptor databases, and the code repository are available online at https://github.com/yyx5048/ Cubic-Perovskite-WorkFunction.

Conflicts of interest

The authors declare no competing conflicts of interest.

Acknowledgements

Y. X. and I. D. acknowledge primary financial support from the National Science Foundation under grant DMREF-1729338. W. C. acknowledges support from the National Science Foundation under grant DMR-2011839 through the MRSEC Center for Nanoscale Science of the Pennsylvania State University. The computational work was performed using the Roar supercomputer of the Penn State Institute for Computational and Data Sciences.

Notes and references

- 1 S. Yamamoto, Rep. Prog. Phys., 2005, 69, 181-232.
- 2 I. E. Castelli, F. Hüser, M. Pandey, H. Li, K. S. Thygesen, B. Seger, A. Jain, K. A. Persson, G. Ceder and K. W. Jacobsen, Adv. Energy Mater., 2015, 5, 1400915.

Paper

- 3 A. K. Singh, J. H. Montoya, J. M. Gregoire and K. A. Persson, Nat. Commun., 2019, 10, 443.
- 4 Y. Xiong and I. Dabo, Phys. Rev. Mater., 2019, 3, 065801.
- 5 S. Trasatti, J. Electroanal. Chem. Interfacial Electrochem., 1972, 39, 163-184.
- 6 A. R. Zeradjanin, A. Vimalanandan, G. Polymeros, A. A. Topalov, K. J. J. Mayrhofer and M. Rohwerder, Phys. Chem. Chem. Phys., 2017, 19, 17019-17027.
- 7 Y. Song, D. Johnson, R. Peng, D. K. Hensley, P. V. Bonnesen, L. Liang, J. Huang, F. Yang, F. Zhang, R. Qiao, A. P. Baddorf, T. J. Tschaplinski, N. L. Engle, M. C. Hatzell, Z. Wu, D. A. Cullen, H. M. Meyer, B. G. Sumpter and A. J. Rondinone, Sci. Adv., 2018, 4(4), e1700336.
- 8 J. Hwang, R. R. Rao, L. Giordano, Y. Katayama, Y. Yu and Y. Shao-Horn, Science, 2017, 358, 751-756.
- 9 T. Liu, C. Xi, C. Dong, C. Cheng, J. Qin, S. Hu, H. Liu and X.-W. Du, J. Phys. Chem. C, 2019, 123, 28319-28326.
- 10 R. E. Schaak and T. E. Mallouk, Chem. Mater., 2002, 14, 1455-1471.
- 11 L. Zhang, Y. Zhou, L. Guo, W. Zhao, A. Barnes, H.-T. Zhang, C. Eaton, Y. Zheng, M. Brahlek, H. F. Haneef, N. J. Podraza, M. H. W. Chan, V. Gopalan, K. M. Rabe and R. Engel-Herbert, Nat. Mater., 2016, 15, 204-210.
- 12 R. C. Haislmaier, E. D. Grimley, M. D. Biegalski, J. M. LeBeau, S. Trolier-McKinstry, V. Gopalan and R. Engel-Herbert, Adv. Funct. Mater., 2016, 26, 7271-7279.
- 13 R. Tran, X.-G. Li, J. H. Montoya, D. Winston, K. A. Persson and S. P. Ong, Surf. Sci., 2019, 687, 48-55.
- 14 R. Jacobs, J. Booske and D. Morgan, Adv. Funct. Mater., 2016, 26, 5471-5482.
- 15 C. Oses, C. Toher and S. Curtarolo, Nat. Rev. Mater., 2020, 5, 295-309.
- 16 J. G. N. Z. J. N. M. Q. T. H. K. V. Sicong Jiang and T. H. J. Luo, Scr. Mater., 2018, 142, 116-120.
- 17 N. A. Benedek and C. J. Fennie, J. Phys. Chem. C, 2013, 117, 13339-13349.
- 18 I. E. Castelli and K. W. Jacobsen, Model. Simul. Mater. Sci. Eng., 2014, 22, 055007.
- 19 A. A. Emery and C. Wolverton, Sci. Data, 2017, 4, 170153.
- 20 G. Pizzi, A. Cepellotti, R. Sabatini, N. Marzari and B. Kozinsky, Comput. Mater. Sci., 2016, 111, 218-230.
- 21 J. P. Perdew, K. Burke and M. Ernzerhof, Phys. Rev. Lett., 1996, 77, 3865.
- 22 P. Giannozzi, S. Baroni, N. Bonini, M. Calandra, R. Car, C. Cavazzoni, D. Ceresoli, G. L. Chiarotti, M. Cococcioni and I. Dabo, et al., J. Condens. Matter Phys., 2009, 21, 395502.
- 23 A. M. Rappe, K. M. Rabe, E. Kaxiras and J. Joannopoulos, Phys. Rev. B: Condens. Matter Mater. Phys., 1990, 41, 1227.
- 24 H. J. Monkhorst and J. D. Pack, Phys. Rev. B: Solid State, 1976, 13, 5188.
- 25 N. Marzari, D. Vanderbilt, A. De Vita and M. Payne, Phys. Rev. Lett., 1999, 82, 3296.
- 26 O. Andreussi and N. Marzari, Phys. Rev. B: Condens. Matter Mater. Phys., 2014, 90, 245101.
- 27 I. Dabo, B. Kozinsky, N. E. Singh-Miller and N. Marzari, Phys. Rev. B: Condens. Matter Mater. Phys., 2008, 77, 115139.

- 28 Y. Li and I. Dabo, Phys. Rev. B: Condens. Matter Mater. Phys., 2011, 84, 155127.
- 29 N. E. Singh-Miller and N. Marzari, Phys. Rev. B: Condens. Matter Mater. Phys., 2009, 80, 235407.
- 30 A. Stroppa and G. Kresse, New J. Phys., 2008, 10, 063020.
- 31 Z. Guo, F. Ambrosio, W. Chen, P. Gono and A. Pasquarello, Chem. Mater., 2018, 30, 94-111.
- 32 T. Ma, R. Jacobs, J. Booske and D. Morgan, APL Mater., 2020, 8,071110.
- 33 S. A. Chambers and P. V. Sushko, Phys. Rev. Mater., 2019, 3, 125803.
- 34 A. V. Krukau, O. A. Vydrov, A. F. Izmaylov and G. E. Scuseria, J. Chem. Phys., 2006, 125, 224106.
- 35 A. Liaw and M. Wiener, R News, 2002, 2, 18-22.
- 36 S. R. Safavian and D. Landgrebe, IEEE Trans. Syst. Man Cybern., 1991, 21, 660-674.
- 37 S. Weisberg, Applied linear regression, John Wiley & Sons, 2005, vol. 528.
- 38 L. Breiman, Mach. Learn., 2001, 45, 5-32.
- 39 J. H. Friedman, Ann. Stat., 2001, 29, 1189-1232.
- 40 J. Schmidt, J. Shi, P. Borlido, L. Chen, S. Botti and M. A. L. Marques, Chem. Mater., 2017, 29, 5090-5103.
- 41 A. van Roekeghem, J. Carrete, C. Oses, S. Curtarolo and N. Mingo, Phys. Rev. X, 2016, 6, 041061.
- 42 G. Pilania, A. Mannodi-Kanakkithodi, B. P. Uberuaga, R. Ramprasad, J. E. Gubernatis and T. Lookman, Sci. Rep., 2016, 6, 19375.
- 43 S. Lu, Q. Zhou, Y. Ouyang, Y. Guo, Q. Li and J. Wang, Nat. Commun., 2018, 9, 3405.
- 44 V. Stanev, C. Oses, A. G. Kusne, E. Rodriguez, J. Paglione, S. Curtarolo and I. Takeuchi, npj Comput. Mater., 2018, 4, 29.
- 45 J. H. Montoya, A. D. Doyle, J. K. Nørskov and A. Vojvodic, Phys. Chem. Chem. Phys., 2018, 20, 3813-3818.
- 46 Y.-L. Lee, J. Kleis, J. Rossmeisl, Y. Shao-Horn and D. Morgan, Energy Environ. Sci., 2011, 4, 3966-3970.
- 47 A. Zunger, Phys. Rev. B: Condens. Matter Mater. Phys., 1980, 22, 5839-5872.
- 48 D. Pettifor, Solid State Commun., 1984, **51**, 31–34.
- 49 L. M. Ghiringhelli, J. Vybiral, S. V. Levchenko, C. Draxl and M. Scheffler, Phys. Rev. Lett., 2015, 114, 105503.
- 50 L. Ward, A. Agrawal, A. Choudhary and C. Wolverton, npj Comput. Mater., 2016, 2, 16028.
- 51 F. Ren, L. Ward, T. Williams, K. J. Laws, C. Wolverton, J. Hattrick-Simpers and A. Mehta, Sci. Adv., 2018, 4(4), eaaq1566.
- 52 W. Li, R. Jacobs and D. Morgan, Comput. Mater. Sci., 2018, **150**, 454-463.
- 53 F. Pedregosa, G. Varoquaux, A. Gramfort, V. Michel, B. Thirion, O. Grisel, M. Blondel, P. Prettenhofer, R. Weiss, V. Dubourg, J. Vanderplas, A. Passos, D. Cournapeau, M. Brucher, M. Perrot and E. Duchesnay, J. Mach. Learn. Res., 2011, 12, 2825-2830.
- 54 Z. Zhong and P. Hansmann, Phys. Rev. B, 2016, 93, 235116.
- 55 S. Halas and T. Durakiewicz, *Vacuum*, 2010, **85**, 486–488.
- 56 T. T. Mayeshiba and D. D. Morgan, Solid State Ionics, 2016, 296, 71-77.
- 57 B. Han, M. Risch, Y.-L. Lee, C. Ling, H. Jia and Y. Shao-Horn, Phys. Chem. Chem. Phys., 2015, 17, 22576-22580.
- 58 R. Jacobs, J. Hwang, Y. Shao-Horn and D. Morgan, Chem. Mater., 2019, 31, 785-797.